# Yolk-shell structured $V_2O_3$ microspheres wrapped in N, S co-doped carbon as pea-pod nanofibers for high-capacity lithium ion batteries

Wenwen Gou[a,1], Xiangzhong Kong[a,1], Yaping Wang[a,*], Yanling Ai[a], Shuquan Liang[a], Anqiang Pan[a,*], Guozhong Cao[b]

[a] School of Materials Science & Engineering, Central South University, Changsha, Hunan 410083, China
[b] Department of Materials Science & Engineering, University of Washington, Seattle, WA 98195, USA

## HIGHLIGHTS

- Pea-pod structured $V_2O_3$/carbon fiber network were successfully fabricated.
- $V_2O_3$ yolk-shell microspheres were wrapped into N, S co-doped carbon framework.
- PAN acts as both electrospinning polymer and carbon/nitrogen sources.
- The obtained composite exhibits excellent electrochemical performances.

## ARTICLE INFO

## ABSTRACT

High-capacity anode materials are widely studied for rechargeable batteries, which have the capability of storing more Li$^+$ ions per formula. However, they normally experience large volume expansion and suffer inferior cycling stability. Herein, we propose pea-pod structured $V_2O_3$ yolk-shell microspheres@N, S co-doped carbon fiber network as an excellent anode material for lithium ion batteries. The prepared vanadium dioxide precursor is uniformly embedded into the carbon fibers by electrospinning treatment and further converted into $V_2O_3$ yolk-shell microspheres during the calcination process. The conductive carbon fiber framework which links $V_2O_3$ microspheres enhanced the electrical conductivity and structural stability significantly. Moreover, the co-doped N and S atoms derived from polymer could produce extrinsic defects, thereby improving Li$^+$ diffusion and electrochemical active sites. When used as anodes for lithium ion batteries, the composite exhibits a high reversible capacity (793.7 mA h g$^{-1}$ after 100 cycles at 100 mA g$^{-1}$), excellent rate performance and cycle stability.

## 1. Introduction

The usage of large quantities of fossil fuels has been a monumental issue for creating serious environmental pollution which threatens the life of humans and other living organisms [1–8]. To avoid the fast consumption fuels, many countries take serious efforts to replace conventional fuel vehicles by electric vehicles. One of the issues with electric vehicles is their endurance which is based on the employed battery system. Lithium ion batteries (LIBs) are considered to be one of the most promising alternatives due to their obvious advantages such as long cycle life, excellent electrochemical performance, low cost and environmentally friendly [9–16]. Until now, the most widely used anode material is graphite. Nevertheless, its low theoretical capacity

(372 mA h g$^{-1}$) limited its further applications for next generation batteries with high energy and power densities [17,18].

Transition metal oxides (TMOs) have drawn extensive attention as anode materials in view of their high theoretical capacities compared to commercialized carbon-based materials [19–24]. Among them, vanadium trioxides ($V_2O_3$) are considered as a promising alternative electrode material for LIBs due to its low cost, abundant resource and high theoretical capacity (1070 mA h g$^{-1}$) [19–25]. However, $V_2O_3$ suffers from the drawbacks of the insufficient intrinsic electronic conductivity, low lithium ion diffusion coefficiency and the large volume variation during the repeated lithiation/delithiation process, which cause the inferior rate capability and cycling stability. Combining transition metal oxides with carbon to make the composites has been proven to be

---

* Corresponding authors.
  *E-mail addresses:* yapingwang@csu.edu.cn (Y. Wang), pananqiang@csu.edu.cn (A. Pan).
  [1] These authors contributed equally to this work.

an efficient strategy to suppress above-mentioned drawbacks [26–28]. In these composites, the carbons function as fast electron transportation media and make the composite structure more stable. To date, many $V_2O_3$/carbon composites have been reported to improve the electrochemical performance of the composites at different extent. Zhang *et al.* [25] reported the reduced graphene oxide (rGO) modified $V_2O_3$ as anode material for LIBs. The $V_2O_3$-rGO composite exhibited higher capacity and better cycle stability than bare $V_2O_3$ particles. An *et al.* [24] fabricated $V_2O_3$ and KB carbon nanocomposites as anode materials for LIBs and sodium ion battery.

More recently, heteroatom doping (such N and S) has recently emerged as an effective strategy to tailor and enhance the physical and chemical properties of carbonaceous materials [29–34]. The incorporation of heteroatoms can enhance the electronic conductivity of carbon, thereby accelerating the electron transport of carbonaceous materials. Moreover, the structural engineering of transition metal oxides, such as core-shell, multi-shell and hollow structures, is another effective strategy to suppress the volume changes upon repeated cycles [35,36]. Therefore, it would be interesting to make the TMOs and heteroatom-doped carbon composites, which can both improve the electronic conductivity and structural stability. Electrospinning is a facile and efficient approach to fabricate continuous carbon nanofibers with good uniformity [37,38]. Meanwhile, the heteroatom contained in polymer can be introduced into carbon fibers during carbonization.

Herein, we successfully synthesized yolk-shell structured $V_2O_3$ microspheres@N, S co-doped carbon pea-pod structured nanofibers network by electrospinning followed by subsequent carbonization and sulfur doping process. The $V_2O_3$ yolk-shell microspheres are uniformly embedded into N, S co-doped carbon fibers network to form network structure. The 1D CNFs construct a continuous conductive network and facilitate the formation of stable SEI film. Core-shell structure accommodates the volume changes of $V_2O_3$ during repeated cycling. As anodes for LIBs, the composite exhibits excellent reversible capacity, long-term cycling stability and good rate capability.

## 2. Experimental section

### 2.1. Material synthesis

The vanadium dioxide microspheres were firstly prepared by our previous report [39]. In a typical synthesis, $V_2O_5$ (1.2 g) and $H_2C_2O_4 \cdot 2H_2O$ in a molar ratio of 1:3 were dissolved in 40 mL of deionized water under vigorous stirring at 80 °C for several hours until a clear blue solution ($VOC_2O_4$) was formed. 2 mL of such obtained solution was then mixed with 30 mL of isopropanol and transferred into a 50 mL Teflon container. The container was sealed in a stainless-steel autoclave and moved to an electrical oven, heated at 200 °C for 2.5 h. After cooling down to room temperature naturally, the resulting black precipitate was collected by centrifugation and washed with absolute ethanol for three times and finally dried at 60 °C overnight. For the synthesis of $V_2O_3$/carbon nanofibers, 0.6 g of obtained $VO_2$ microspheres were firstly dispersed into 2 mL of N, N-Dimethylformamide (DMF, AR, 99.5%) by ultrasound for 0.5 h. Then 0.2 g Polyacrylonitrile (PAN, $M_w$ = 1500000) was added into the solution and stirred continuously for 24 h. After that, the obtained homogeneous viscous black dispersion was introduced into a 5 mL plastic syringe equipped with a stainless-steel needle (20 G), which was connected to a high voltage supply via a metal clip. A flat stainless-steel plate covered with a layer of aluminum foil was acted as the collector of nanofibers. Important parameter settings in the spinning process are summarized below: distance between needle tip and the collector is 15 cm and the direct current voltage was set as 12 kV, with a feeding rate of 0.7 mL h$^{-1}$.

The as-spun precursors were stabilized in a muffle furnace at 250 °C for 1 h with a heating rate of 3 °C min$^{-1}$. To obtain N, S co-doped CNFs encapsulating $V_2O_3$ network (noted as $V_2O_3$@NSCNFs), the stabilized precursors and sulfur powders (mass ratio, 1:3) were mixed together

and annealed in 5% $H_2$/95% Ar at 600 °C for 5 h with a heating rate of 3 °C min$^{-1}$. For comparison, we also prepared pure CNFs, N-doped $V_2O_3$ (noted as $V_2O_3$@NCNFs) by electrospinning and pure $V_2O_3$ microspheres.

### 2.2. Materials characterization

The crystalline structures of all $V_2O_3$@CNF composites and CNFs were investigated by X-ray diffraction (XRD, Rigaku D/max 2500) with Cu Kα radiation collected in the range of 2θ = 10 ~ 80° at a scanning rate of 8° min$^{-1}$. X-ray photoelectron spectroscopy (XPS) was used to further analyze the surface chemistry of samples recorded on the ESCALAB 250Xi. The morphology and microstructures of the samples were characterized by scanning electron microscopy (SEM, Nova NanoSEM230) and transition electron microscopy (TEM, JEOL JEM-2100F). Raman spectrometer (LabRAM HR800) and Fourier transform infrared radiation (FT-IR) were used for the corresponding characterization of carbon fibers and possible residual organic functional groups (Nicolet 6700).

### 2.3. Electrochemical measurement

The electrodes were prepared through the typical method. Briefly, as-prepared samples were mixed with carbon black (Super P) and sodium carboxymetheyl cellulose (CMC) at the weight ratio of 80:10:10. After grinding for 20 min, the mixture was evenly dispersed in DI water to form a slurry, which was coated on copper foil and dried in a vacuum oven at 80 °C overnight. The electrode was punched into cells with a diameter of 12 mm, the mass loading of active material per electrode is approximately 1 mg cm$^{-2}$. All the 2016 type coin cells were assembled in a glove box (Mbraun, Germany) filled with high purity argon. The lithium metal foil was used as counter electrode, 1 mol L$^{-1}$ LiPF$_6$ in a mixture of ethyl carbonate (EC), dimethyl carbonate (DMC) and diethyl carbonate (DEC) (1:1:1 v:v:v) as the electrolyte, and polypropylene membrane as the separator. After standing for 12 h, the galvanostatic charge and discharge performance of the electrodes were evaluated by a Land Battery Tester (Land CT 2001A, Wuhan, China) in the voltage range between 0.01 and 3 V (vs. Li/Li$^+$) at room temperature. Cyclic Voltammetry (CV; 0.01–3.0 V) measurements were carried out on an electrochemical workstation (CHI660E, China).

## 3. Results and discussion

Scheme 1 illustrates the formation of $V_2O_3$@NSCNFs via $VO_2$ microspheres by electrospinning. As shown in the schematic representation, $VO_2$ microspheres and PAN polymer were uniformly dispersed in DMF solution by ultrasonication and continuous magnetic stirring to form a uniform dispersion. Then the obtained dispersion was transformed into $VO_2$-PAN precursor by electrospinning. During this process, the $VO_2$ microspheres are wrapped by PAN polymers to form a Pea-Pod like structure. After vulcanization (S) in $H_2$/Ar atmosphere, the inner $VO_2$ microspheres are in situ converted into $V_2O_3$, whereas the extrinsic polymer shells are transformed into N-doped carbon layers. The PAN polymer works as a linker of Pea-Pod structure, and also functions as source for both carbon and nitrogen. The carbon-coated $V_2O_3$ core-shell structure can greatly improve the structural stability of the electrode material.

Fig. 1a shows the XRD patterns of the CNFs, $V_2O_3$ core-shell microspheres and $V_2O_3$@NSCNFs composite. After annealing under $H_2$/Ar atmosphere, the polymer fibers are converted to CNFs. The corresponding XRD pattern shows a broad diffraction peak at 23.6°, which can be ascribed to (0 0 2) plane of amorphous carbon. For monodisperse core-shell microspheres obtained from solvothermal and annealing process, all the diffraction peaks located at 24.3°, 32.9°, 36.2°, 53.9°, 65.1° can be indexed to the (0 1 2), (1 0 4), (1 1 0), (1 1 6), (3 0 0) planes of rhombohedral-phase crystalline $V_2O_3$ (JCPDS: 034–0187),
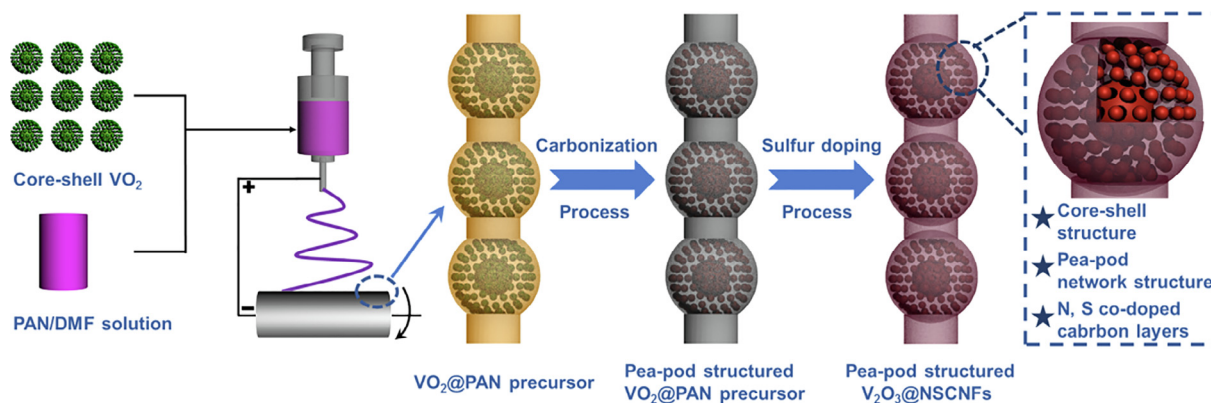
**Scheme 1.** Schematic illustrations of the fabrication of $V_2O_3$@NSCNFs composite.

respectively. No other residual peaks are detected, indicating the successful synthesis of pure $V_2O_3$ phase. For $V_2O_3$@NSCNFs, diffraction peaks of both carbon and $V_2O_3$ are detected, confirming the existence of $V_2O_3$ and CNFs. In addition, the weaker peak intensity than that of pure $V_2O_3$ could be attributed to the presence of amorphous CNFs, since it reduces the crystallization of $V_2O_3$@CNF composite. Besides, XRD pattern of $V_2O_3$@NCNFs is displayed in Fig. S3. All the diffraction peaks can be indexed to planes of rhombohedral-phase crystalline $V_2O_3$ (JCPDS: 034-0187), which also demonstrates the successfully synthesis of $V_2O_3$ phase.

In order to investigate the complete conversion of PAN into $V_2O_3$@CNFs, Fourier transform infrared radiation (FT-IR) measurement was carried out. As shown in Fig. 1b, the peak at $982\,cm^{-1}$ represents the existence of $V^{3+}=O$, which belongs to $V_2O_3$, in agreement with

the XRD result. Besides, the absorptions at 1310, 1570, 2360 and $3420\,cm^{-1}$ are due to water and nitrate adsorbed on the KBr and can be ignored. No obvious peaks of organic functional groups are observed in FT-IR spectra, confirming that the $VO_2$-PAN precursor has been completely converted into $V_2O_3$@NSCNFs.

Raman spectroscopy test was conducted to investigate the in depth information on carbon fiber composition of the $V_2O_3$@NSCNFs and the result is shown in Fig. 1c. The peaks located at 141, 283, 689 and $989\,cm^{-1}$ can be ascribed to the characteristic peaks of $V_2O_3$ [40]. Other two characteristic bands of carbonaceous materials located at $1347\,cm^{-1}$ (D-band, disordered carbon) and $1579\,cm^{-1}$ (G-band, graphene carbon) are also clearly detected (inset in Fig. 1c). The intensity ratio of the D-band to the G-band ($I_D/I_G$) is 1.17, which confirms the existence of low crystallinity carbon with an amorphous structure in the
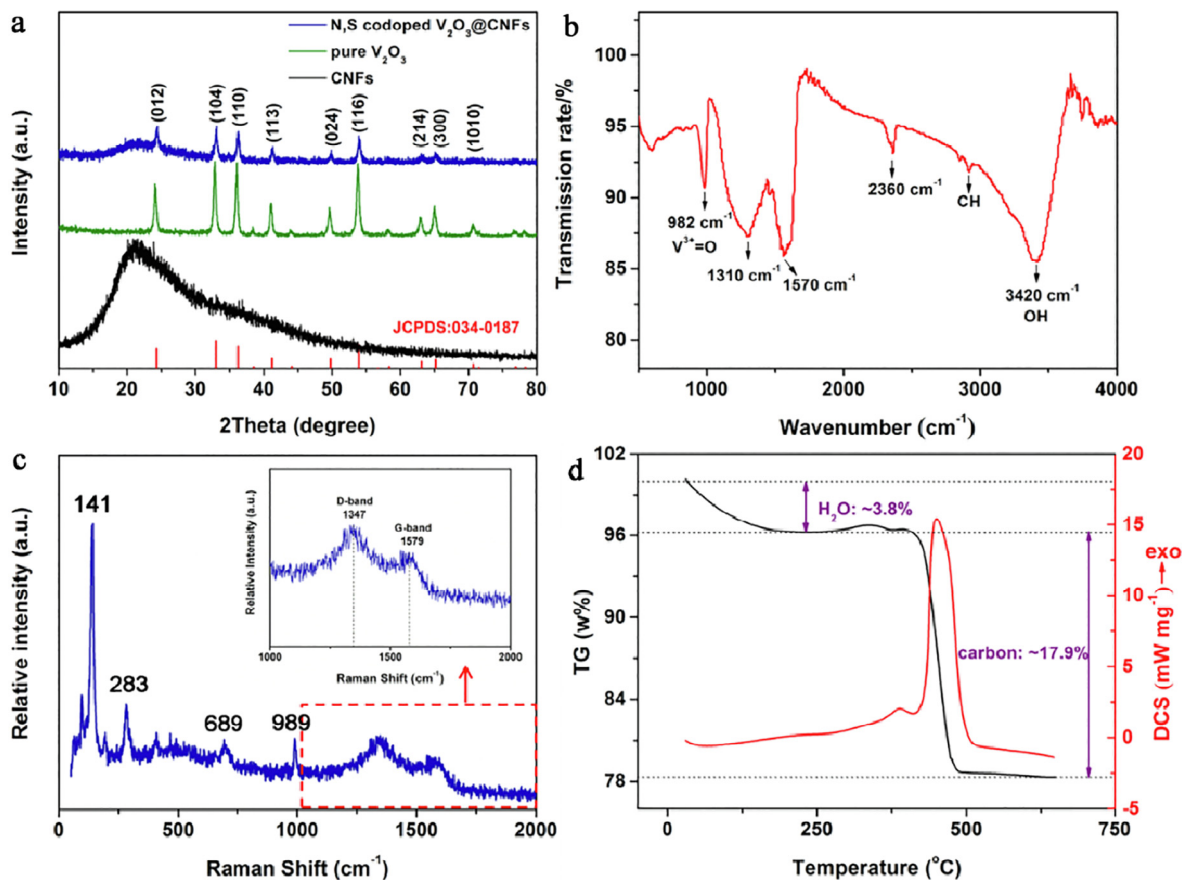


**Fig. 1.** (a) XRD patterns of annealed carbon fibers, pure vanadium trioxide microspheres and $V_2O_3$@NSCNF composites. (b) FT-IR spectra. (c) Raman scattering patterns of $V_2O_3$@NSCNF composites. (d) TG and DSC curves of the $V_2O_3$@NSCNFs composite.

composites. Raman spectrum of V$_2$O$_3$@NCNFs, pure V$_2$O$_3$ and pure CNFs are displayed in Fig. S4. As the result shown, the characteristic bands of V$_2$O$_3$@NCNFs and V$_2$O$_3$ are consistent with V$_2$O$_3$@NSCNFs, meanwhile the intensity ratio of D-band to the G-band ($I_D/I_G$) of pure CNFs and V$_2$O$_3$@NCNFs are 1.24 and 1.25, respectively.

Thermogravimetric analysis (TGA) of V$_2$O$_3$@NSCNFs composite was conducted to investigate the mass content of V$_2$O$_3$ in the composite. As shown in Fig. 1d, the temperature rose from room temperature to 650 °C with a heating rate of 10 °C min$^{-1}$ in air, initial decrease in quality can be attributed to the evaporation of physical water adsorbed in the sample, the subsequent slight increase in mass is ascribed to the oxidation of V$_2$O$_3$ to V$_2$O$_5$ in air. Approximately 17.9% of the weight loss between 400 and 500 °C was caused by the consumption of carbon fibers in the composite. Finally, the weight kept constant due to the burning out of CNFs and complete conversion of V$_2$O$_3$ to V$_2$O$_5$. From the obtained result, the mass content of V$_2$O$_3$ in the composites is calculated to be 64.6%.

BET characterizations were carried out to detect the pore structures of CNFs, V$_2$O$_3$@NCNFs, and V$_2$O$_3$@NSCNFs. Fig. S5 shows the nitrogen adsorption-desorption isotherm curves and corresponding pore size distribution of (a, b) CNFs, (c, d) V$_2$O$_3$@NCNFs, (e, f) V$_2$O$_3$@NSCNFs, which possess specific surface areas of 12.66 m$^2$ g$^{-1}$, 7.92 m$^2$ g$^{-1}$, and 25.65 m$^2$ g$^{-1}$, respectively, indicating the enlarged surface area after vulcanization. The introduction of heteroatoms can create large defects in carbon structure, which helps to enhance the adsorption of lithium ions and conductivity of active materials.

Field emission scanning electron microscopy (FESEM) was used to characterize as-prepared V$_2$O$_3$@CNF composites. As shown in Fig. S1, it is clearly observed that the solvothermal precursor presents as rough microspheres with a diameter of about 1 μm. Statistical analysis was conducted to get the average diameter shown in Fig. S6, the result in Fig. S6 indicates that their size ranged from 0.4 to 1.8 μm. Fig. S7 shows SEM images of pure V$_2$O$_3$ which present as rough surface microspheres, indicating the structure of precursor is well maintained during the conversion process. Moreover, obvious core-shell structure can be found in TEM images (Fig. S2). The morphology and interior structure of V$_2$O$_3$@NSCNFs are shown in Fig. 2, According to Fig. 2a and b, all the V$_2$O$_3$ microspheres are evenly embedded in the carbon fibers network and are arranged neatly and no extra V$_2$O$_3$ microspheres out of CNFs are detected. SEM images of pure CNFs and V$_2$O$_3$@NCNFs are displayed in Fig. S8. As shown in Fig. S8a and b, pure CNFs exhibits a smooth surface and an extremely uniform size, while V$_2$O$_3$@NCNFs possess pea-pod like structure (Fig. S8c and d) which is similar to V$_2$O$_3$@NSCNFs.

The interior nanostructure of V$_2$O$_3$@NSCNF composites were further investigated by transmission electron microscopy (TEM). Fig. 2d shows that a single V$_2$O$_3$ microsphere with a core-shell structure is just embedded in the middle of the carbon fiber and the V$_2$O$_3$ microsphere has a diameter of about 1 μm, which is consistent with the results of the SEM images (Fig. S1). As shown in Fig. 2e and f, the high-resolution TEM (HRTEM) image shows a crystal structure with obvious lattice fringes of ~0.27 nm, which is agree with the d-spacing of (1 0 4) planes of rhombohedral-phase crystalline V$_2$O$_3$, again demonstrating the existence of V$_2$O$_3$ in the composite. The corresponding element mapping images (Fig. 2g–l) indicate the uniform distribution of C, N and S elements in the fiber. The segregation of vanadium and oxygen at the fiber node indicates the presence of V$_2$O$_3$ core-shell microsphere.

X-ray photoelectron spectroscopy (XPS) was conducted to obtain information about the elemental composition and chemical status of the as-prepared samples. As shown in Fig. 3a, the survey scan clearly revealed the presence of V, O, C, N and S. XPS spectrum of C 1s (Fig. 3b) was divided into three peaks located at 284.7, 285.6 and 286.9 eV correspond to the binding energies of C−C bond, C−N/C−S bond and C−O bond [41], respectively. The peaks of N 1s (Fig. 3c) could be resolved into 398.4, 399.8, 400.7 and 404.1 eV, which are assigned to pyridinic N, pyrrolic N, graphitic N and oxidized N [42], respectively. The O 1s spectrum (Fig. 3d) shows two main peaks located at 530.5 and 531.5 eV ascribed to V−O bond and C−O bond, respectively, confirming that the as-prepared samples are pure vanadium oxide. Fig. 3e displays the high-resolution S 2p spectrum, three distinct characteristic peaks indicate the existence of C-S 2p$_{3/2}$ bond (163.8 eV), C=S 2p$_{1/2}$ bond (165.1 eV) and oxidized S (168.7 eV) [30,43], respectively. In addition, the high-resolution V 2p spectrum is shown in Fig. 3f, two characteristic peaks at 517.5 and 524.3 eV can be indexed to V$^{3+}$ 2p$_{3/2}$ and 2p$_{1/2}$, respectively, the peak at 516.5 eV observed in the XPS spectrum of V 2p can be attributed to V$^{4+}$ [40]. The results indicate that some V$_2$O$_3$ microspheres have been partially oxidized. Obviously, the doping of N and S atoms on carbon fiber is successful. Co-doped heteroatoms could produce a large number of defects and active sites on the surface of carbon fibers, which helps to enhance the adsorption of lithium ion and conductivity of active materials.

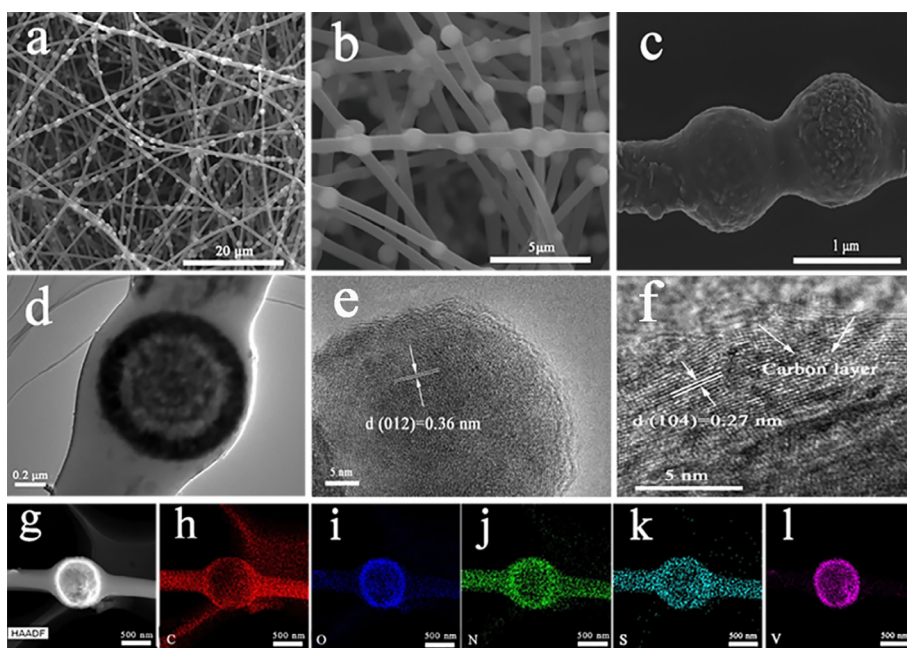Fig. 4a shows the initial three successive CV curves of the V$_2$O$_3$@



**Fig. 2.** (a-c) SEM images of different magnifications. (d) TEM and (e, f) HRTEM images of the V$_2$O$_3$@NSCNFs. (g-l) The corresponding elemental mapping results for C (red), O (blue), N (green), S (medium yellow) and V (magenta). (For interpretation of the references to colour in this figure legend, the reader is referred to the web version of this article.)
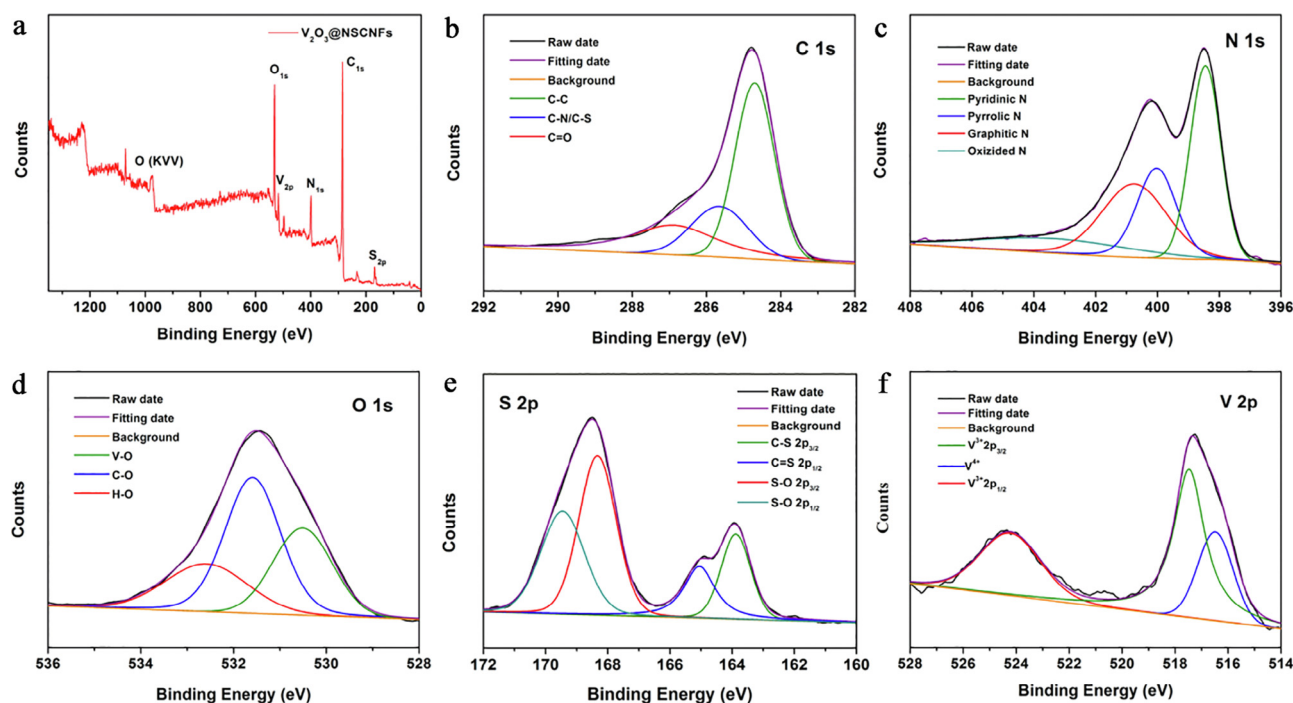
**Fig. 3.** (a) XPS survey scan, high-resolution XPS of (b) C 1s, (c) N 1s, (d) O 1s, (e) S 2p, (f) V 2p for $V_2O_3$@NSCNFs.

NSCNFs in the voltage range of 0.01–3 V vs. Li/Li$^+$ at a scan rate of 0.1 mV s$^{-1}$. During the first cathode scan, there is a significant reduction peak at 0.16 V which disappeared in the next scans, corresponding to the insertion of lithium ions and the formation of SEI films. $V_2O_3$ was

reduced to metal vanadium. In the anode scan, two broad peaks were recorded at 1.25 V and 2.64 V, respectively, which can be attributed to the subsequent oxidation reaction process. Interestingly, there is a distinct oxidation peak at 1.75 V, which is a sulfur reaction [44],
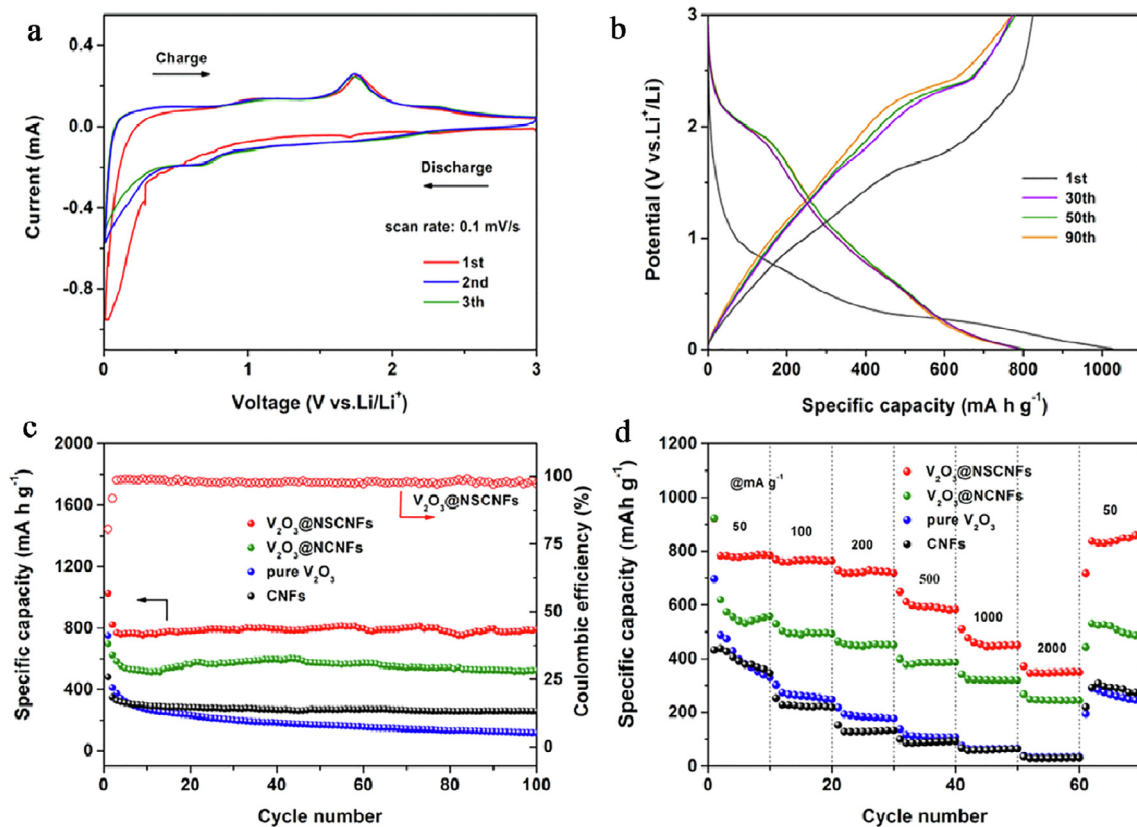


**Fig. 4.** Electrochemical performances of the $V_2O_3$@NSCNFs, pure $V_2O_3$ microspheres, $V_2O_3$@NCNFs and CNFs in the window of 0.01–3 V (vs. Li/Li$^+$). (a) CV curves of the $V_2O_3$@NSCNFs at a voltage scan rate of 0.1 mV s$^{-1}$; (b) Charge-discharge curves for the 1st, 30th, 50th, 90th cycles at a current density of 100 mA g$^{-1}$; (c) Cycling performance and coulombic efficiency of the four electrode materials at a current density of 100 mA g$^{-1}$; (d) Rate capacities at various current densities.

**Table 1**
The electrochemical performance of pea-pod structural $V_2O_3$@NSCNFs works as anode material of LIBs and previous reports.

| Anode material | Test voltage | Discharge capacity (mAh g$^{-1}$) | Cycle numbers | References |
|---|---|---|---|---|
| Yolk–shell $V_2O_3$ | 0.01–3 V | 437.5 (100 mA g$^{-1}$) | 100 | [20] |
| $V_2O_3$/CNF nano-felts | 0.01–3 V | 500 (100 mA g$^{-1}$) | 100 | [48] |
| $V_2O_3$/KB carbon | 0.01–3 V | 587 (100 mA g$^{-1}$) | 200 | [24] |
| $V_2O_3$rGO | 0.01–3 V | 380 (100 mA g$^{-1}$) | 50 | [49] |
| $V_2O_3$/CNF | 0.01–3 V | 544 (500 mA g$^{-1}$) | 500 | [50] |
| This work | 0.01–3 V | 793.7 (100 mA g$^{-1}$) | 100 | — |

indicating that sulfur doping can significantly improve the battery capacity not only by increasing the active site on the surface of the compound, but also for the storage of Li$^+$ reaction, by participating in the redox reaction. The second and third cycle of the CV curves overlap closely, indicating good reversibility of the $V_2O_3$@NSCNFs during the electrochemical reaction. The Li$^+$ intercalation process can be described as follows [45–47]:

$$V_2O_3 + xLi^+ + xe^- \leftrightarrow 2Li_xV_2O_3 \tag{1}$$

$$Li_xV_2O_3 + (6-x)Li^+ + (6-x)e^- \leftrightarrow 2\,V + 3Li_2O \tag{2}$$
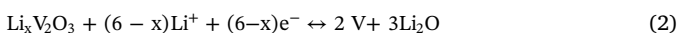
XPS spectrum of $V_2O_3$@NSCNFs at fully discharged state was conducted to further investigate the change of valence state of components in the electrochemical process. The high resolution XPS spectra of V 2p for fresh and fully discharged $V_2O_3$@NSCNFs electrodes are shown in Fig. S9a, which exhibit similar profiles. However, the position of V 2p peak after full discharge obviously shift to low energy region, suggesting the reduction of $V^{3+}$ to low-valent vanadium. High resolution spectrum of S 2p (Fig. S9b) demonstrates two peaks located at 163.8 and 165.1 eV are corresponding to C—S and C=S bond, which is weakened significantly after fully discharged process. testifying the reaction of doping S and Li.

To further test the electrochemical performance of the $V_2O_3$@NSCNF composites as an anode material for lithium-ion batteries, a galvanostatic charge-discharge cycle test was conducted. Fig. 4b presents the charge and discharge curves of the selected cycles at 100 mA g$^{-1}$ between 0.01 and 3.0 V for the composites. The storage mechanism of lithium ions during discharge is composed of two steps: the insertion process and the conversion reaction. When the voltage is between 1.0 and 0.5 V, the intermediate product of $Li_xV_2O_3$ is formed during the insertion process, resulting in a gradual decrease of the discharge plateau. Due to the conversion reaction of $V_2O_3$, there is a discharge plateau around 0.5 V. The composite has a specific discharge capacity of 1025.6 mA g$^{-1}$ for the first cycle, the corresponding charging specific capacity is 825.2 mA h g$^{-1}$, and the coulombic efficiency is 80.5%, which is much higher than pure $V_2O_3$. The irreversibility of capacity is attributed to the formation of SEI film and irreversible phase transformation. The subsequent charge and discharge curves are close to coincide, indicating that the material retains a relatively complete structure and high lithium ion storage capacity after 100 cycles. Fig. S10a illustrates the $V_2O_3$@NSCNFs electrode possesses higher current densities than pure $V_2O_3$, indicating its better electrochemical reactivity due to the introduction of CNFs shell. Additionally, as shown in Fig. S10b, the $V_2O_3$@NSCNFs electrode exhibits higher discharge and lower charge plateaus than pure $V_2O_3$, suggesting its lower polarization as well as better reactivity. Besides, the larger slope of the discharge profile indicates more capacitive behavior during lithium ion storage.

Fig. 4c shows the cycling performance of the obtained samples at a current density of 100 mA g$^{-1}$. For $V_2O_3$@NSCNFs, discharge specific capacity is 793.7 mA h g$^{-1}$ after 100 cycles, which is even slightly higher than that of the 3th cycle (767.3 mA h g$^{-1}$) and no obvious capacity fading or rising are detected, indicating good cycle stability.

However, pure $V_2O_3$ delivers a capacity of only 115.7 mA h g$^{-1}$ after 100 cycles with a capacity retention of 28%. Serious capacity fading of pure $V_2O_3$ may be attributed to the destruction of the $V_2O_3$ microspheres during the cycle. This result demonstrates that conductive carbon network can effectively enhance the cycling stability of $V_2O_3$. Despite good cycling stability, $V_2O_3$@NCNFs exhibits lower reversible capacity (576 mA h g$^{-1}$) than that of $V_2O_3$@NSCNFs, suggesting that N, S co-doping improves the reversible capacity of $V_2O_3$@CNFs. CNFs exhibit a specific discharge capacity of 280 mA h g$^{-1}$ with good cycling stability. The electrochemical performance of NSCNFs electrode is also tested to evaluate the effect of S-doping and shown in Fig. S11. NSCNFs exhibit a specific discharge capacity of 439.7 mA h g$^{-1}$ with good cycling stability, much higher than pure CNFs. Fig. S12 presents the long cycling performance of $V_2O_3$@NSCNFs and a stable capacity of 420 mA h g$^{-1}$ was available after 500 cycles even at 500 mA h g$^{-1}$, indicating practical prospects for fast charge electrodes. The comparison between our work and previous reports based on $V_2O_3$ is shown in Table 1 and the result shows that the advantages of pea-pod like nanostructure.

To further evaluate the electrochemical properties of electrodes, rate performance of the obtained samples is shown in Fig. 4d, $V_2O_3$@NSCNFs exhibits the highest specific capacity and optimal rate performance. The discharge specific capacities of 787.4, 767.2, 725.9, 594.1, 449.5, and 350.5 mA h g$^{-1}$ are exhibited at a current density of 50, 100, 200, 500, 1000, and 2000 mA g$^{-1}$, respectively. When current density is returned to 50 mA g$^{-1}$, the capacity is 830.9 mA h g$^{-1}$, even higher than that of the initial cycles, which is attributed to the activation of electrodes. The results show that $V_2O_3$@NSCNFs has the best rate performance as anode materials for LIBs. Based on the electrochemical properties mentioned above, $V_2O_3$@NSCNFs exhibits the highest discharge specific capacity, optimum rate performance and cycle stability. The enhanced Li$^+$ storage capability for the composite electrode can be attribute to the coherent synergistic effect of $V_2O_3$ and CNFs as well as the doping of heteroatoms. Carbon fiber can improve the electrical conductivity of the electrode material and maintain the structural stability of the material during the cycle. The doping of heteroatoms increases the active site of the material, and the sulfur atom itself participates in the lithium storage reaction. Area capacity of synthetic electrode was calculated and shown in Fig. S13. The cell delivered a capacity of $\sim 0.7$ mA h cm$^{-2}$ at 0.088 mA cm$^{-2}$ (0.1 C) reveals good practical application potential.

To investigate the structural stability of the electrode, A flexible electrode was directly assembled into Li-ion batteries without milling and disclosed after 100 cycles at 100 mA g$^{-1}$, the SEM and TEM results are shown in Fig. S14. The intact and continuous structure of the $V_2O_3$@NSCNFs can be reserved, demonstrating the good structural stability. As shown in TEM image, many nanoparticles are uniformly encapsuled in carbon fiber after cycling indicating carbon shell can effectively protect $V_2O_3$.

The electrochemical impedance spectroscopy (EIS) measurements were carried out to study the charge transfer resistance of the electrodes. Nyquist plots of $V_2O_3$@NSCNFs, $V_2O_3$@NCNFs, pure CNFs and pure $V_2O_3$, and the $V_2O_3$@NSCNFs after 100 cycles (inset: the corresponding equivalent circuit) are shown in Fig. S15. The curves of all samples consist of a semi-circle in the high frequency region represents charge transfer resistance (Rct) and a linear slope in the low frequency region indicates the Warburg impedance (Zw). The $V_2O_3$@NSCNFs electrode exhibits smallest charge transfer resistance (116.9 $\Omega$), which contributes to the faster reaction kinetics and higher capacity as a result of both vertical and horizontal conductive paths for faster electron transportation networks. The increasing charge-transfer resistance after cycle (190 $\Omega$) can be ascribed to the formation of fractured SEI layers and slight damage to the surface structure of the $V_2O_3$@NSCNFs electrode.

Galvanostatic Intermittent Titration Technique (GITT) was used to measure the lithium diffusion coefficient (Fig. S16). The obtained GITT
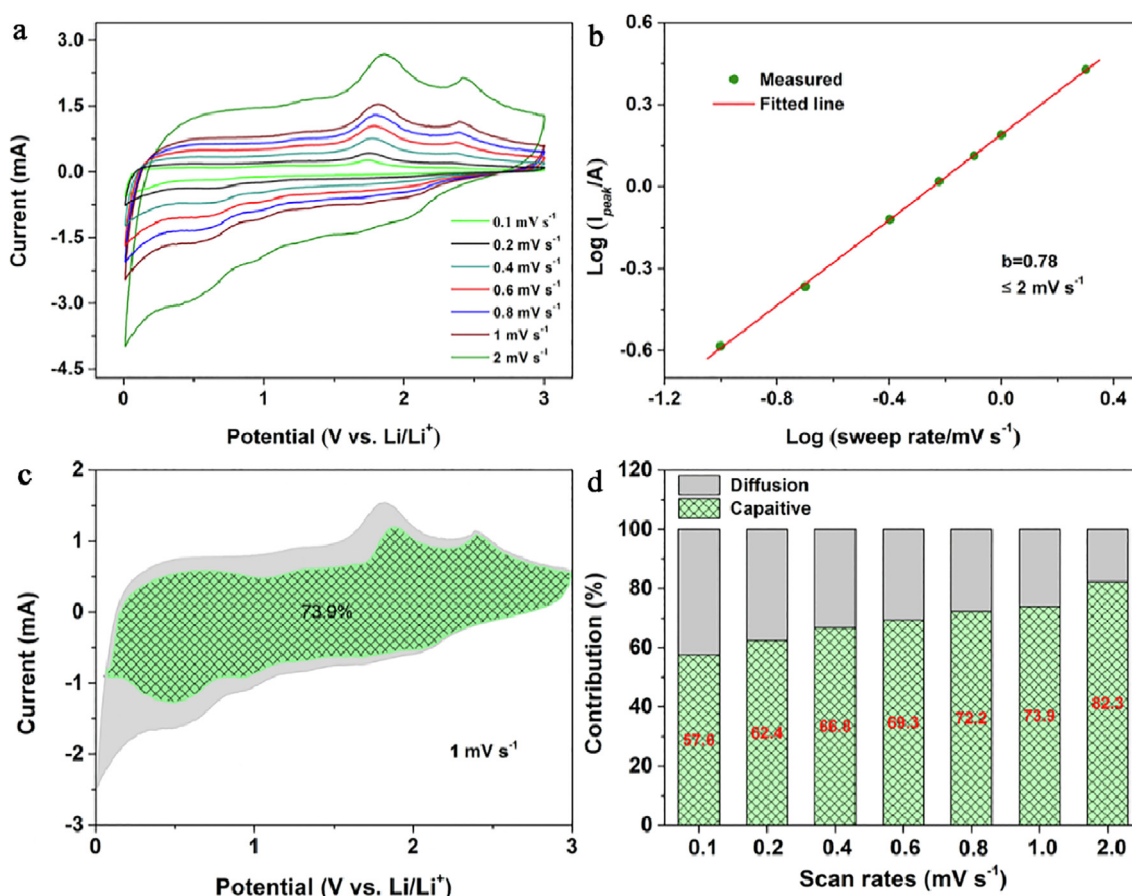
**Fig. 5.** (a) CV curves of $V_2O_3$@NSCNFs at different scan rates from $0.1\,mV\,s^{-1}$ to $2.0\,mV\,s^{-1}$. (b) log(i) versus log(v) plots of cathodic current maxima on $V_2O_3$ electrodes. (c) CV curve of composite with separation between the total current (solid line) and pseudocapacitive current (shaded region) at $1\,mV\,s^{-1}$. (d) Comparison of the capacity with pseudocapacitive contribution at 0.1, 0.2, 0.4, 0.6, 0.8, 1 and $2\,mV\,s^{-1}$.

curves and *D* values at various lithiation/delithiation states for $V_2O_3$@NSCNFs electrodes are shown in Fig. S17. The *D* in the $V_2O_3$@NSCNFs ranges from $3.8 \times 10^{-9}$ to $1.1 \times 10^{-8}\,cm^2\,s^{-1}$ during the electrochemical process. The high lithium ion diffusivity is mainly attributed to the rational design of the pea-pod like network structure. Sulfur doping provides many mesoporous channels and active sites for fast ion diffusion.

Lithium storage processes can be divided into two main types, namely ion diffusion and surface induced capacitance processes. In order to investigate the contribution of capacitive charge and intercalated charge, a kinetic analysis was conducted for a half-cell. The CV curves at various scan rates from 0.1 to $2\,mV\,s^{-1}$ were tested. And as shown in Fig. 5a, a representative feature that current (i) at a permanent voltage increases with sweep rate. The slight voltage shift at different sweep indicates that the polarization of the electrodes is small at higher rates. According to the literatures [51–53], and have a relationship given by equations:

$$i = a\nu^b \tag{3}$$

$$\log i = b\log \nu + \log a \tag{4}$$

where a and b are adjustable parameters. When the b value approaches to 0.5, it indicates that ion diffusion dominates the charge and discharge process, while the b value approaches to 1, it represents the ideal capacitive behavior. By drawing a diagram and fitting a straight line, the b value is calculated by determining the slope to study the charge storage mechanism. As shown in Fig. 5b, the calculated b value is 0.78, indicating that the redox process of $V_2O_3$ has partial pseudocapacitive behavior. This part of the pseudocapacitive behavior helps to promote the insertion and extraction of lithium ions at high rates and

improve rate performance. According to previous literature reports [54,55], the ratio between diffusion control and capacitive charge storage can be further quantified. The current (i) at a permanent voltage can be expressed by

$$i = k_1\nu + k_2\nu^{0.5} \tag{5}$$

where $k_1\nu$ and $k_2\nu^{0.5}$ represent the contribution of pseudocapacitive and ion diffusion, respectively. According to the calculation results in Fig. 5c and d, the capacitance contributions of pseudocapacitive at sweep rates of 0.1, 0.2, 0.4, 0.6, 0.8, 1, and $2\,mV\,s^{-1}$ are 57.8%, 62.4%, 66.8%, 69.4%, 72.2%, 73.9% and 82.3%, respectively. This indicates that the surface induced capacitance process plays an important role in the capacity of the composite, especially in terms of rate performance. At the same time, the contribution of the ion diffusion process decreases with sweep rate, which can be attributed to the slower embedding speed cannot satisfy the high speed electrochemical process [56].

## 4. Conclusion

In summary, $V_2O_3$@NSCNFs was synthesized via a combined hydrothermal and electrospinning method followed by subsequent calcination process. The $V_2O_3$ microspheres were uniformly embedded in the NSCNFs to form pea-pod structure. As anodes of LIBs, $V_2O_3$@NSCNFs exhibited good cycling stability ($793.7\,mA\,h\,g^{-1}$ after 100 cycles at a current density of $100\,mA\,g^{-1}$), as well as good rate capability. Enhanced electrochemical performance is attributed to the synergistic effect of carbon fibers and $V_2O_3$, the doping of heteroatoms is also crucial.

## Acknowledgments

## Appendix A. Supplementary data

Supplementary data to this article can be found online at https://doi.org/10.1016/j.cej.2019.05.144.

## References

[1] S. Chu, A. Majumdar, Opportunities and challenges for a sustainable energy future, Nature 488 (2012) 294–303.

[2] A. Midilli, I. Dincer, Hydrogen as a renewable and sustainable solution in reducing global fossil fuel consumption, Int. J. Hydrogen Energy 33 (2008) 4209–4222.

[3] S. Planton, M. Déqué, F. Chauvin, L. Terray, Expected impacts of climate change on extreme climate events, C.R. Geosci. 340 (2008) 564–574.

[4] M. Pudukudy, Z. Yaakob, M. Mohammad, B. Narayanan, K. Sopian, Renewable hydrogen economy in Asia-Opportunities and challenges: an overview, Renew. Sustain. Energy Rev. 30 (2014) 743–757.

[5] M.F. Ruth, O.R. Zinaman, M. Antkowiak, R.D. Boardman, R.S. Cherry, M.D. Bazilian, Nuclear-renewable hybrid energy systems: opportunities, interconnections, and needs, Energy Convers. Manage. 78 (2014) 684–694.

[6] E. Shafiei, B. Davidsdottir, J. Leaver, H. Stefansson, E.I. Asgeirsson, Comparative analysis of hydrogen, biofuels and electricity transitional pathways to sustainable transport in a renewable-based energy system, Energy 83 (2015) 614–627.

[7] M.M. Thackeray, C. Wolverton, E.D. Isaacs, Electrical energy storage for transportation—approaching the limits of, and going beyond, lithium-ion batteries, Energy Environ. Sci. 5 (2012) 7854.

[8] E. Uchaker, Y.Z. Zheng, S. Li, S.L. Candelaria, S. Hu, G.Z. Cao, Better than crystalline: amorphous vanadium oxide for sodium-ion batteries, J. Mater. Chem. A 2 (2014) 18208–18214.

[9] Y.K. Sun, Z. Chen, H.J. Noh, D.J. Lee, H.G. Jung, Y. Ren, S. Wang, C.S. Yoon, S.T. Myung, K. Amine, Nanostructured high-energy cathode materials for advanced lithium batteries, Nat. Mater. 11 (2012) 942–947.

[10] Y. Tang, Y. Zhang, W. Li, B. Ma, X. Chen, Rational material design for ultrafast rechargeable lithium-ion batteries, Chem. Soc. Rev. 44 (2015) 5926–5940.

[11] X. Wang, Y. Huang, D. Jia, W.K. Pang, Z. Guo, Y. Du, X. Tang, Y. Cao, Self-assembled sandwich-like vanadium oxide/graphene mesoporous composite as high-capacity anode material for lithium ion batteries, Inorg. Chem. 54 (2015) 11799–11806.

[12] M. Yan, F. Wang, C. Han, X. Ma, X. Xu, Q. An, L. Xu, C. Niu, Y. Zhao, X. Tian, P. Hu, H. Wu, L. Mai, Nanowire templated semihollow bicontinuous graphene scrolls: designed construction, mechanism, and enhanced energy storage performance, J. Am. Chem. Soc. 135 (2013) 18176–18182.

[13] P. Yan, J. Zheng, J. Xiao, C.-M. Wang, J.-G. Zhang, Recent advances on the understanding of structural and composition evolution of LMR cathodes for Li-ion batteries, Front. Energy Res. 3 (2015).

[14] Y. Yao, M.T. McDowell, I. Ryu, H. Wu, N. Liu, L. Hu, W.D. Nix, Y. Cui, Interconnected silicon hollow nanospheres for lithium-ion battery anodes with long cycle life, Nano Lett. 11 (2011) 2949–2954.

[15] G. Zhang, X.W. Lou, General synthesis of multi-shelled mixed metal oxide hollow spheres with superior lithium storage properties, Angew. Chem. 53 (2014) 9041–9044.

[16] J. Zheng, M. Gu, A. Genc, J. Xiao, P. Xu, X. Chen, Z. Zhu, W. Zhao, L. Pullan, C. Wang, J.G. Zhang, Mitigating voltage fade in cathode materials by improving the atomic level uniformity of elemental distribution, Nano Lett. 14 (2014) 2628–2635.

[17] N.A. Kaskhedikar, J. Maier, ChemInform abstract: lithium storage in carbon nanostructures, Cheminform 40 (2009) 2664–2680.

[18] W. Sun, G. Gao, K. Zhang, Y. Liu, G. Wu, Self-assembled 3D N-CNFs/V₂O₅ aerogels with core/shell nanostructures through vacancies control and seeds growth as an outstanding supercapacitor electrode material, Carbon 132 (2018) 667–677.

[19] H. Jiang, G. Jia, Y. Hu, Q. Cheng, Y. Fu, C. Li, Ultrafine V₂O₃ nanowire embedded in carbon hybrids with enhanced lithium storage capability, Ind. Eng. Chem. Res. 54 (2015) 2960–2965.

[20] L. Jiang, Y. Qu, Z. Ren, P. Yu, D. Zhao, W. Zhou, L. Wang, H. Fu, In situ carbon-coated yolk-shell V₂O₃ microspheres for lithium-ion batteries, ACS Appl. Mater. Interfaces 7 (2015) 1595–1601.

[21] Y. Sun, S. Jiang, W. Bi, C. Wu, Y. Xie, Highly ordered lamellar V₂O₃-based hybrid nanorods towards superior aqueous lithium-ion battery performance, J. Power Sources 196 (2011) 8644–8650.

[22] Y. Zhang, M. Fan, L. Hu, W. Wu, J. Zhang, X. Liu, Y. Zhong, C. Huang, Fabrication of V₂O₃/C core–shell structured composite and VC nanobelts by the thermal treatment of VO₂/C composite, Appl. Surf. Sci. 258 (2012) 9650–9655.

[23] Y. Zhang, N. Wang, Y. Huang, C. Huang, X. Mei, C. Meng, Synthesis of V₂O₃/C composites with different morphologies by a facile route and phase transition properties of the compounds, Mater. Sci.-Poland 32 (2014) 236–242.

[24] X. An, H. Yang, Y. Wang, Y. Tang, S. Liang, A. Pan, G. Cao, Hydrothermal synthesis of coherent porous V₂O₃/carbon nanocomposites for high-performance lithium- and sodium-ion batteries, Sci. China Mater. 60 (2017) 717–727.

[25] Z. Yifang, A. Pan, S. Liang, T. Chen, Y. Tang, X. Tan, Reduced graphene oxide modified V₂O₃ with enhanced performance for lithium-ion battery, Mater. Lett. (2014).

[26] H. Mi, X. Yang, Y. Li, P. Zhang, L. Sun, A self-sacrifice template strategy to fabricate yolk-shell structured silicon@void@carbon composites for high-performance lithium-ion batteries, Chem. Eng. J. 351 (2018) 103–109.

[27] H. Mi, X. Yang, F. Li, X. Zhuang, C. Chen, Y. Li, P. Zhang, Self-healing silicon-sodium alginate-polyaniline composites originated from the enhancement hydrogen bonding for lithium-ion battery: a combined simulation and experiment study, J. Power Sources 412 (2019) 749–758.

[28] F. Luo, D. Ma, Y. Li, H. Mi, P. Zhang, S. Luo, Hollow Co₃S₄/C anchored on nitrogen-doped carbon nanofibers as a free-standing anode for high-performance Li-ion batteries, Electrochim. Acta 299 (2019) 173–181.

[29] B. He, W.-C. Li, A.-H. Lu, High nitrogen-content carbon nanosheets formed using the Schiff-base reaction in a molten salt medium as efficient anode materials for lithium-ion batteries, J. Mater. Chem. A 3 (2015) 579–585.

[30] J. Wang, H. Lu, Q. Hong, Y. Cao, X. Li, J. Bai, Porous N, S-codoped carbon architectures with bimetallic sulphide nanoparticles encapsulated in graphitic layers: highly active and robust electrocatalysts for the oxygen reduction reaction in Al-air batteries, Chem. Eng. J. 330 (2017) 1342–1350.

[31] S. Wang, L. Zhang, Z. Xia, A. Roy, D.W. Chang, J.B. Baek, L. Dai, BCN graphene as efficient metal-free electrocatalyst for the oxygen reduction reaction, Angew. Chem. 51 (2012) 4209–4212.

[32] W. Yang, L. Chen, X. Liu, X. Yue, C. Liu, J. Jia, N, S-Codoped microporous carbon nanobelts with blooming nanoflowers for oxygen reduction, J. Mater. Chem. A 4 (2016) 5834–5838.

[33] J. Ye, J. Zang, Z. Tian, M. Zheng, Q. Dong, Sulfur and nitrogen co-doped hollow carbon spheres for sodium-ion batteries with superior cyclic and rate performance, J. Mater. Chem. A 4 (2016) 13223–13227.

[34] A. Zehtab Yazdi, E.P.L. Roberts, U. Sundararaj, Nitrogen/sulfur co-doped helical graphene nanoribbons for efficient oxygen reduction in alkaline and acidic electrolytes, Carbon 100 (2016) 99–108.

[35] Y.N. Ko, Y. Chan Kang, S.B. Park, A new strategy for synthesizing yolk-shell V₂O₅ powders with low melting temperature for high performance Li-ion batteries, Nanoscale 5 (2013) 8899–8903.

[36] D. Jiao, Y. Liang, Q. Ying, L. Lu, H. Bing, L. Hua, K. Yu, Controlled synthesis of anisotropic hollow ZnCo₂O₄ octahedrons for high-performance lithium storage, Energy Storage Mater. 11 (2018) 184–190.

[37] X. Qin, H. Zhang, J. Wu, X. Chu, Y.-B. He, C. Han, C. Miao, S. Wang, B. Li, F. Kang, Fe₃O₄ nanoparticles encapsulated in electrospun porous carbon fibers with a compact shell as high-performance anode for lithium ion batteries, Carbon 87 (2015) 347–356.

[38] H. Jie, Q. Ying, W. Xiong, L. Qing, L. Ming, X. Yue, D. Da, L. Hua, K. Yu, Electrosprayed porous Fe₃O₄/carbon microspheres as anode materials for high-performance lithium-ion batteries, Nano Res. 2 (2018) 892–904.

[39] A. Pan, H.B. Wu, L. Yu, T. Zhu, X.W. Lou, Synthesis of hierarchical three-dimensional vanadium oxide microstructures as high-capacity cathode materials for lithium-ion batteries, ACS Appl. Mater. Interfaces 4 (2012) 3874–3879.

[40] S. Tan, Y. Jiang, Q. Wei, Q. Huang, Y. Dai, F. Xiong, Q. Li, Q. An, X. Xu, Z. Zhu, X. Bai, L. Mai, Multidimensional synergistic nanoarchitecture exhibiting highly stable and ultrafast sodium-ion storage, Adv. Mater. 30 (2018) e1707122.

[41] H. Park, W. Jae, J. Kim, One-pot synthesis of Li₃VO₄ particles with thin nitrogen-doped carbon coating layers as an anode material for lithium-ion batteries, J. Alloys Compd. 767 (2018) 657–665.

[42] H. Bin, L. Cui, L. Hui, High nitrogen-content carbon nanosheets formed using the Schiff-base reaction in a molten salt medium as efficient anode materials for lithium-ion batteries, J. Mater. Chem. A 3 (2015) 579–585.

[43] G. Zou, C. Wang, H. Hou, C. Wang, X. Qiu, X. Ji, Controllable interlayer spacing of sulfur-doped graphitic carbon nanosheets for fast sodium-ion batteries, Small 13 (2017) 1700762.

[44] J. Sheng, L. Yang, Y.-E. Zhu, F. Li, Y. Zhang, Z. Zhou, Oriented SnS nanoflakes bound on S-doped N-rich carbon nanosheets with a rapid pseudocapacitive response as high-rate anodes for sodium-ion batteries, J. Mater. Chem. A 5 (2017) 19745–19751.

[45] L. Zeng, C. Zheng, J. Xi, H. Fei, M. Wei, Composites of V₂O₃–ordered mesoporous carbon as anode materials for lithium-ion batteries, Carbon 62 (2013) 382–388.

[46] D. Cheng, M. Guang, H. Jun, C. Hua, L. Yang, Polymer-pyrolysis assisted synthesis of vanadium trioxide and carbon nanocomposites as high performance anode materials for lithium-ion batteries, J. Power Sources 261 (2014) 184–187.

[47] W. Yu, Z.J. Hui, A.S. Admar, W.C. Zhong, Cheong, Borgna, L. Yi, Improved cyclability of lithium-ion battery anode using encapsulated v2o3 nanostructures in well-graphitized carbon fiber, RSC Adv. 2 (2013) 5748.

[48] S. Gao, D. Zhang, K. Zhu, J.A. Tang, Z. Gao, Y. Wei, G. Chen, Y. Gao, Flexible V₂O₃/carbon nano-felts as free-standing electrode for high performance lithium ion batteries, J. Alloys Compd. 702 (2017) 13–19.

[49] Y. Zhang, A. Pan, S. Liang, T. Chen, Y. Tang, X. Tan, Reduced graphene oxide modified V₂O₃ with enhanced performance for lithium-ion battery, Mater. Lett. 137 (2014) 174–177.

[50] X. Liu, R. Liu, L. Zeng, X. Huang, X. Chen, C. Zheng, Y. Xu, Q. Qian, M. Wei, Q. Chen, Facile preparation of a V₂O₃/carbon fiber composite and its application for long-term performance lithium-ion batteries, New J. Chem. 41 (2017) 5380–5386.

[51] P.L. Taberna, S. Mitra, P. Poizot, P. Simon, J.M. Tarascon, High rate capabilities Fe₃O₄-based Cu nano-architectured electrodes for lithium-ion battery applications, Nat. Mater. 5 (2006) 567–573.

[52] Y.S. Yun, S.Y. Cho, H. Kim, H.-J. Jin, K. Kang, Ultra-thin hollow carbon nanospheres for pseudocapacitive sodium-ion storage, ChemElectroChem 2 (2015) 359–365.

[53] X. Xu, F. Niu, D. Zhang, C. Chu, C. Wang, J. Yang, Y. Qian, Hierarchically porous Li$_3$VO$_4$/C nanocomposite as an advanced anode material for high-performance lithium-ion capacitors, J. Power Sources 384 (2018) 240–248.

[54] J. Jin, Y. Zheng, L.B. Kong, N. Srikanth, Q. Yan, K. Zhou, Tuning ZnSe/CoSe in MOF-derived N-doped porous carbon/CNTs for high-performance lithium storage, J. Mater. Chem. A 6 (2018) 15710–15717.

[55] G. Zou, H. Hou, G. Zhao, Z. Huang, P. Ge, X. Ji, Preparation of S/N-codoped carbon nanosheets with tunable interlayer distance for high-rate sodium-ion batteries, Green Chem. 19 (2017) 4622–4632.

[56] L. Shen, H. Lv, S. Chen, P. Kopold, P.A. van Aken, X. Wu, J. Maier, Y. Yu, Peapod-like Li$_3$VO$_4$/N-doped carbon nanowires with pseudocapacitive properties as advanced materials for high-energy lithium-ion capacitors, Adv. Mater. 29 (2017).